Supplementary Information

A global decline in atmospheric dust during the 21ˢᵗ century

Ashok Kumar Gupta[1,2], Jasper F. Kok[1], Vassilis Amiridis[3], Antonis Gkikas[4], Konstantinos Rizos[3], Emmanouil Proestakis[3], Stavros Logothetis[7], Eleni Marinou[3] and Carlos Pérez García-Pando[5,6]

[1]Department of Atmospheric and Oceanic Sciences, University of California, Los Angeles, CA, 90095, USA

[2]*Department of Earth and Environmental Sciences, Vanderbilt University, Nashville, TN, USA

[3]Institute for Astronomy, Astrophysics, Space Applications and Remote Sensing, National Observatory of Athens, 15236 Athens, Greece

[4]Research Centre for Atmospheric Physics and Climatology, Academy of Athens, 11521 Athens, Greece

[5]Barcelona Supercomputing Center, Barcelona, Spain

[6]Catalan Institution for Research and Advanced Studies, Barcelona, Spain

[7]Laboratory of Atmospheric Physics, Department of Physics, University of Patras, 26500 Patras, Greece

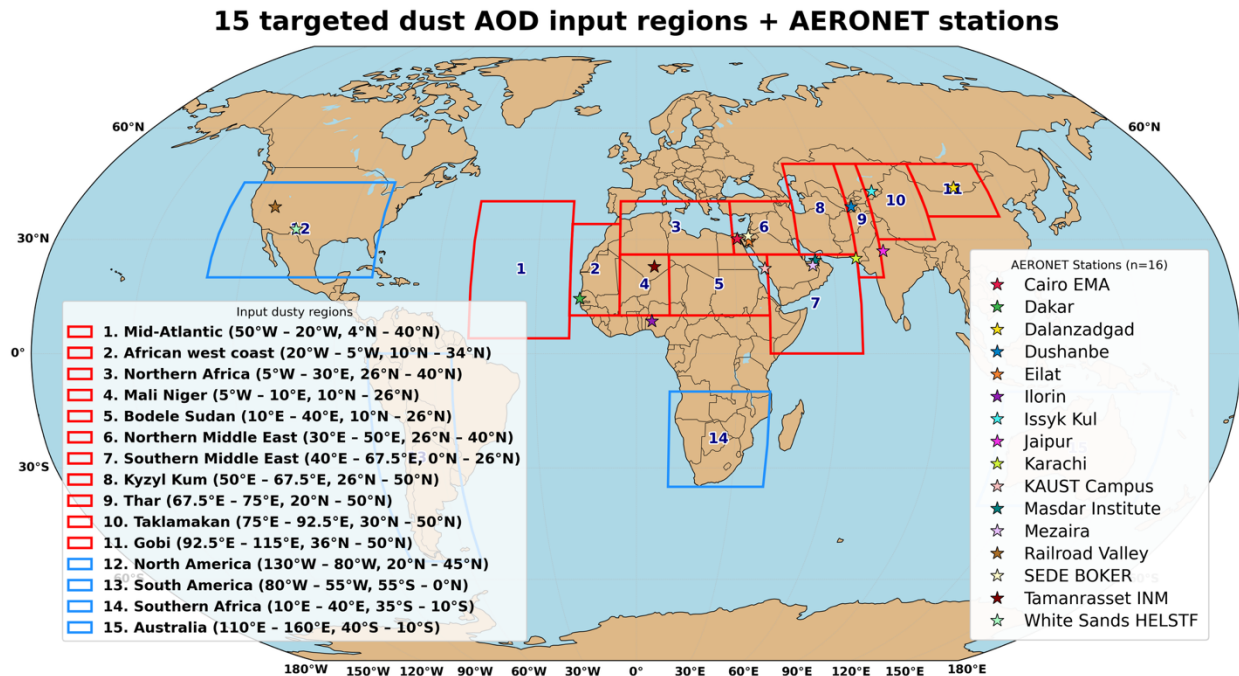*Corresponding author (& present Address): Ashok Kumar Gupta, ashok.k.gupta@vanderbilt.edu

This PDF file includes:
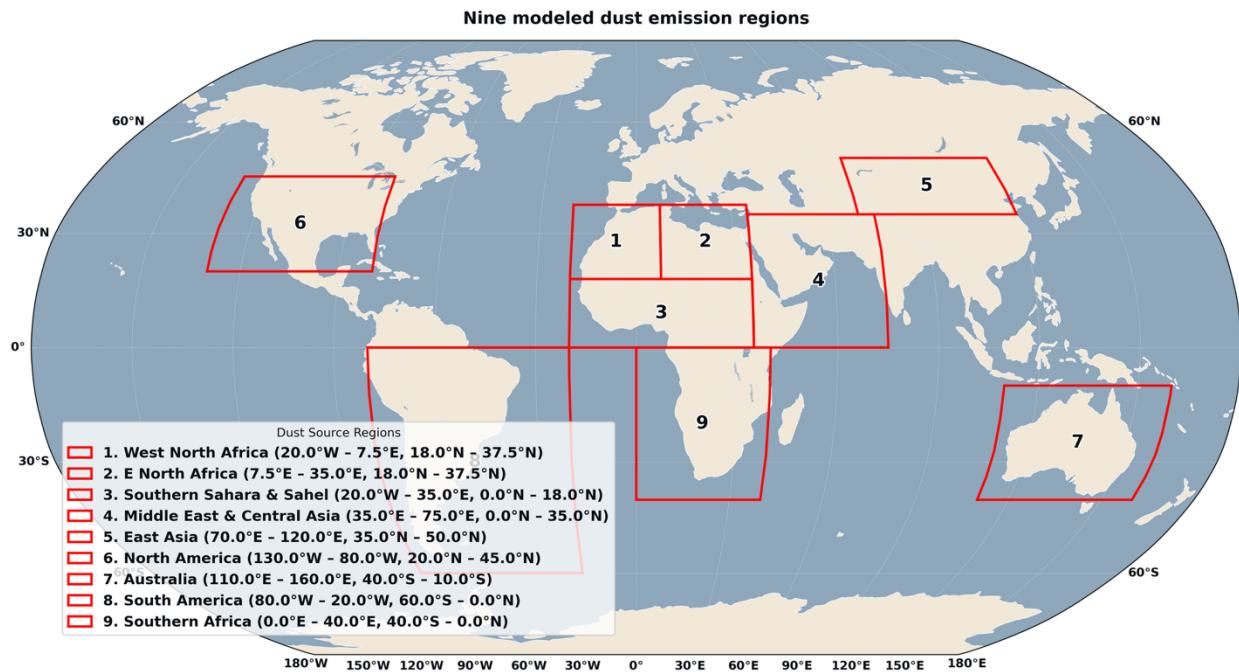
   Supplementary Figures 1-15

   Supplementary Table 1

Supplementary Figures

Supplementary Figure 1

15 targeted dust AOD input regions + AERONET stations

Input dusty regions
- 1. Mid-Atlantic (50°W – 20°W, 4°N – 40°N)
- 2. African west coast (20°W – 5°W, 10°N – 34°N)
- 3. Northern Africa (5°W – 30°E, 26°N – 40°N)
- 4. Mali Niger (5°W – 10°E, 10°N – 26°N)
- 5. Bodele Sudan (10°E – 40°E, 10°N – 26°N)
- 6. Northern Middle East (30°E – 50°E, 26°N – 40°N)
- 7. Southern Middle East (40°E – 67.5°E, 0°N – 26°N)
- 8. Kyzyl Kum (50°E – 67.5°E, 26°N – 50°N)
- 9. Thar (67.5°E – 75°E, 20°N – 50°N)
- 10. Taklamakan (75°E – 92.5°E, 30°N – 50°N)
- 11. Gobi (92.5°E – 115°E, 36°N – 50°N)
- 12. North America (130°W – 80°W, 20°N – 45°N)
- 13. South America (80°W – 55°W, 55°S – 0°N)
- 14. Southern Africa (10°E – 40°E, 35°S – 10°S)
- 15. Australia (110°E – 160°E, 40°S – 10°S)

AERONET Stations (n=16)
- Cairo EMA
- Dakar
- Dalanzadgad
- Dushanbe
- Eilat
- Ilorin
- Issyk Kul
- Jaipur
- Karachi
- KAUST Campus
- Masdar Institute
- Mezaira
- Railroad Valley
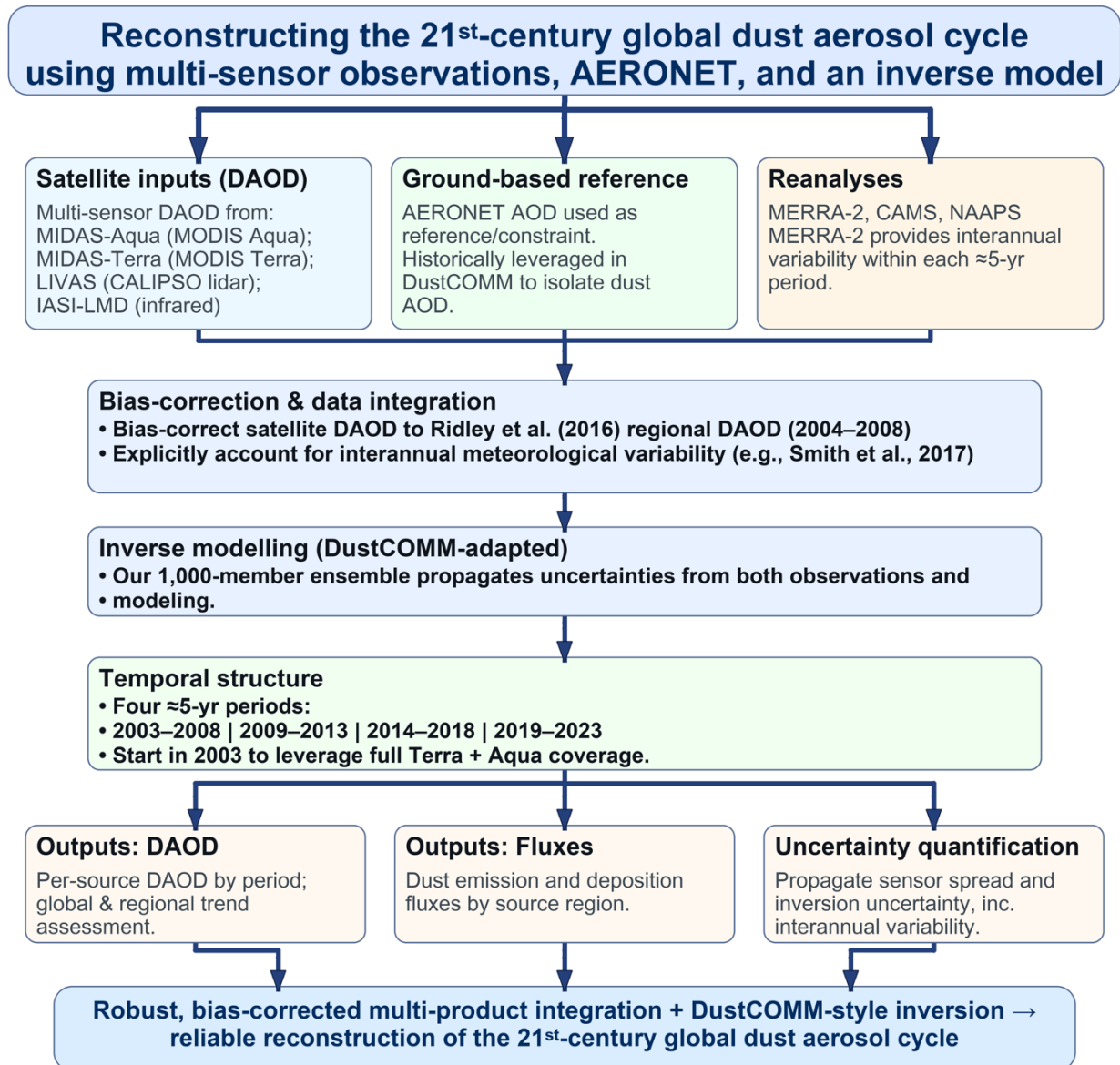- SEDE BOKER
- Tamanrasset INM
- White Sands HELSTF

Supplementary Figure 1: Global distribution of 15 dusty regions used by the inverse model. *Spatial boundaries of the 15 dusty regions for which the regionally averaged DAOD is used in the inverse model (Kok et al., 2021a), delineated based on satellite-derived dust climatologies and prior observational and modeling studies (Ridley et al., 2016). Red boxes denote regions where dust generally dominates the AOD, while blue boxes indicate less dusty regions where dust does not dominate the AOD. The numbered regions correspond to those listed in the accompanying legend, including major dust hotspots such as the Sahara (Regions 3–5), the Middle East (Regions 6–7), Central and East Asia (Regions 8–11), and lesser sources in the Americas, Australia, and southern Africa (Regions 12–15).* The 16 AERONET stations used for trend comparisons are marked with stars.

Supplementary Figure 2

Supplementary Figure 2: Global distribution of 9 modeled dust emission source regions. Map showing the global locations of the nine principal dust emission source regions identified in the study.
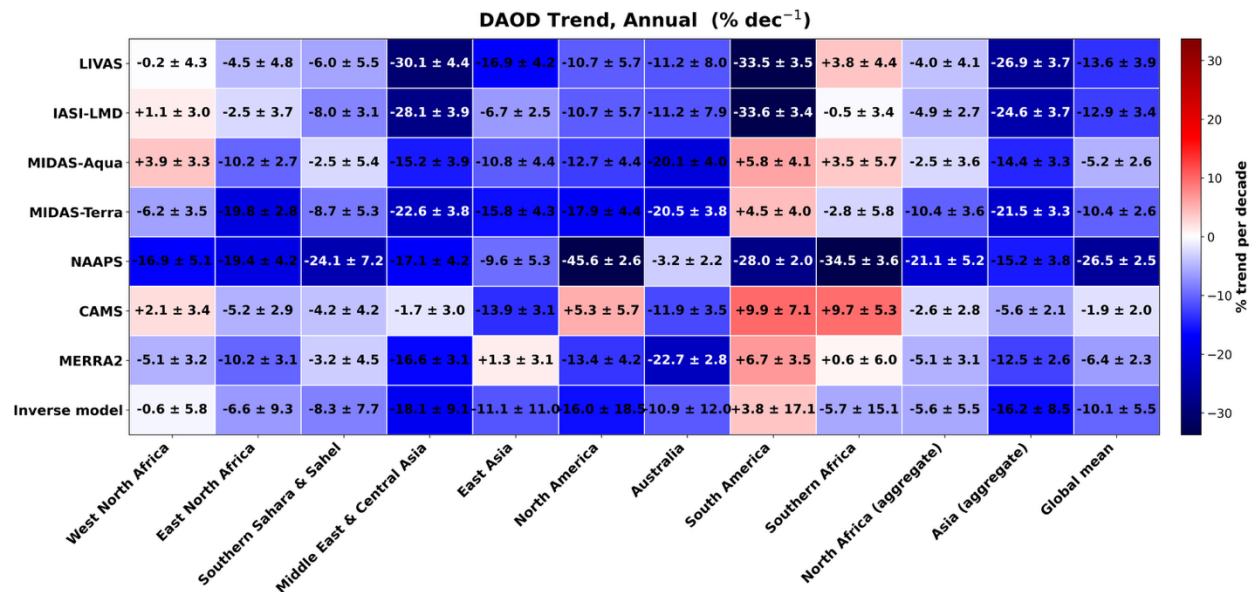
Supplementary Figure 3

Reconstructing the 21st-century global dust aerosol cycle using multi-sensor observations, AERONET, and an inverse model

Satellite inputs (DAOD)
Multi-sensor DAOD from:
MIDAS-Aqua (MODIS Aqua);
MIDAS-Terra (MODIS Terra);
LIVAS (CALIPSO lidar);
IASI-LMD (infrared)

Ground-based reference
AERONET AOD used as
reference/constraint.
Historically leveraged in
DustCOMM to isolate dust
AOD.

Reanalyses
MERRA-2, CAMS, NAAPS
MERRA-2 provides interannual
variability within each ≈5-yr
period.

Bias-correction & data integration
• Bias-correct satellite DAOD to Ridley et al. (2016) regional DAOD (2004–2008)
• Explicitly account for interannual meteorological variability (e.g., Smith et al., 2017)

Inverse modelling (DustCOMM-adapted)
• Our 1,000-member ensemble propagates uncertainties from both observations and
• modeling.

Temporal structure
• Four ≈5-yr periods:
• 2003–2008 | 2009–2013 | 2014–2018 | 2019–2023
• Start in 2003 to leverage full Terra + Aqua coverage.

Outputs: DAOD
Per-source DAOD by period;
global & regional trend
assessment.

Outputs: Fluxes
Dust emission and deposition
fluxes by source region.

Uncertainty quantification
Propagate sensor spread and
inversion uncertainty, inc.
interannual variability.

**Robust, bias-corrected multi-product integration + DustCOMM-style inversion →
reliable reconstruction of the 21st-century global dust aerosol cycle**

Supplementary Figure 3: Methodological framework for reconstructing the 21st century global dust aerosol cycle using satellite, reanalysis, and ground-based observations integrated with an inverse model. The framework integrates multiple satellite-based aerosol datasets (LIVAS, MIDAS-Aqua, MIDAS-Terra, IASI-LMD), ground-based AERONET observations (e.g., Ridley et al., 2016), and three global aerosol reanalysis products (NAAPS, CAMS, MERRA-2). Satellite-derived DAOD trends were evaluated against AERONET coarse-mode AOD observations. Seasonal regional DAOD was extracted from these data sets for 11 major dust-dominated regions and 4 less dusty regions (Supplementary Fig. 1) and used in the DustCOMM inverse model to obtain DAOD, dust loading, dust emission fluxes, and deposition fluxes from 2003 to
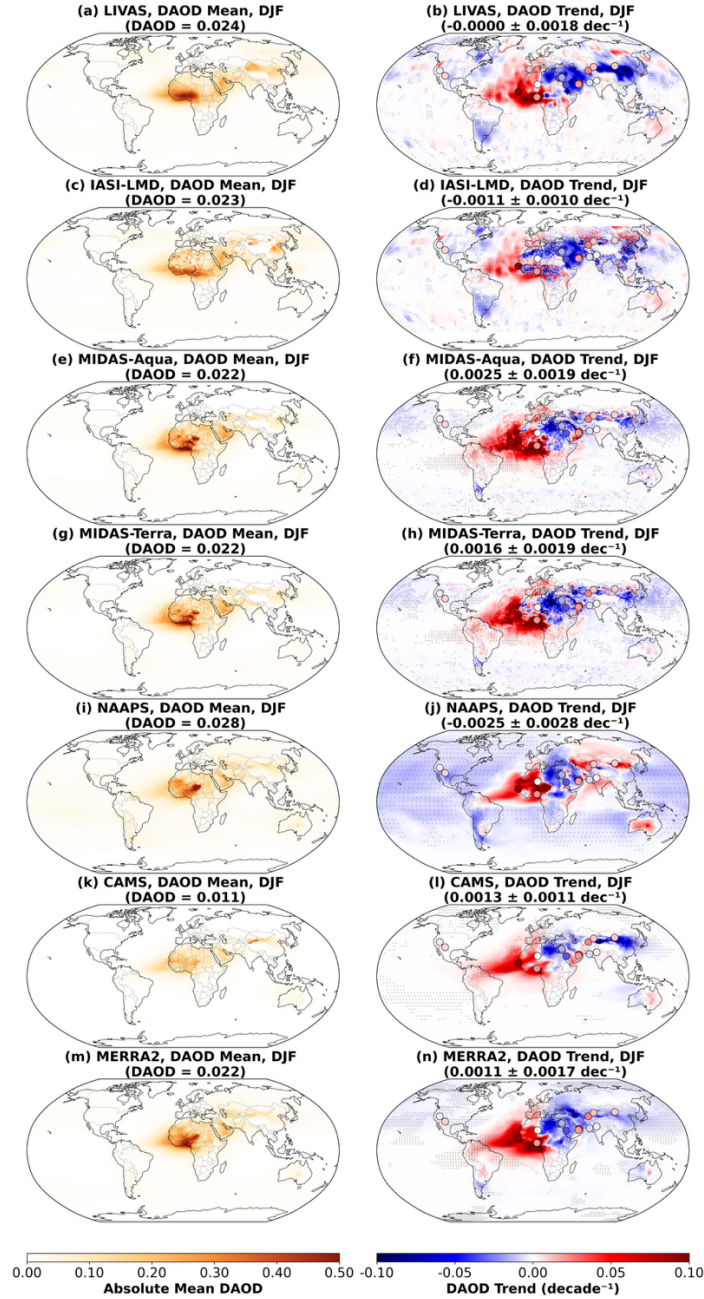
2023. Uncertainties were assessed through the spread of the ensemble of 1000 different bootstrap simulations (see Methods).
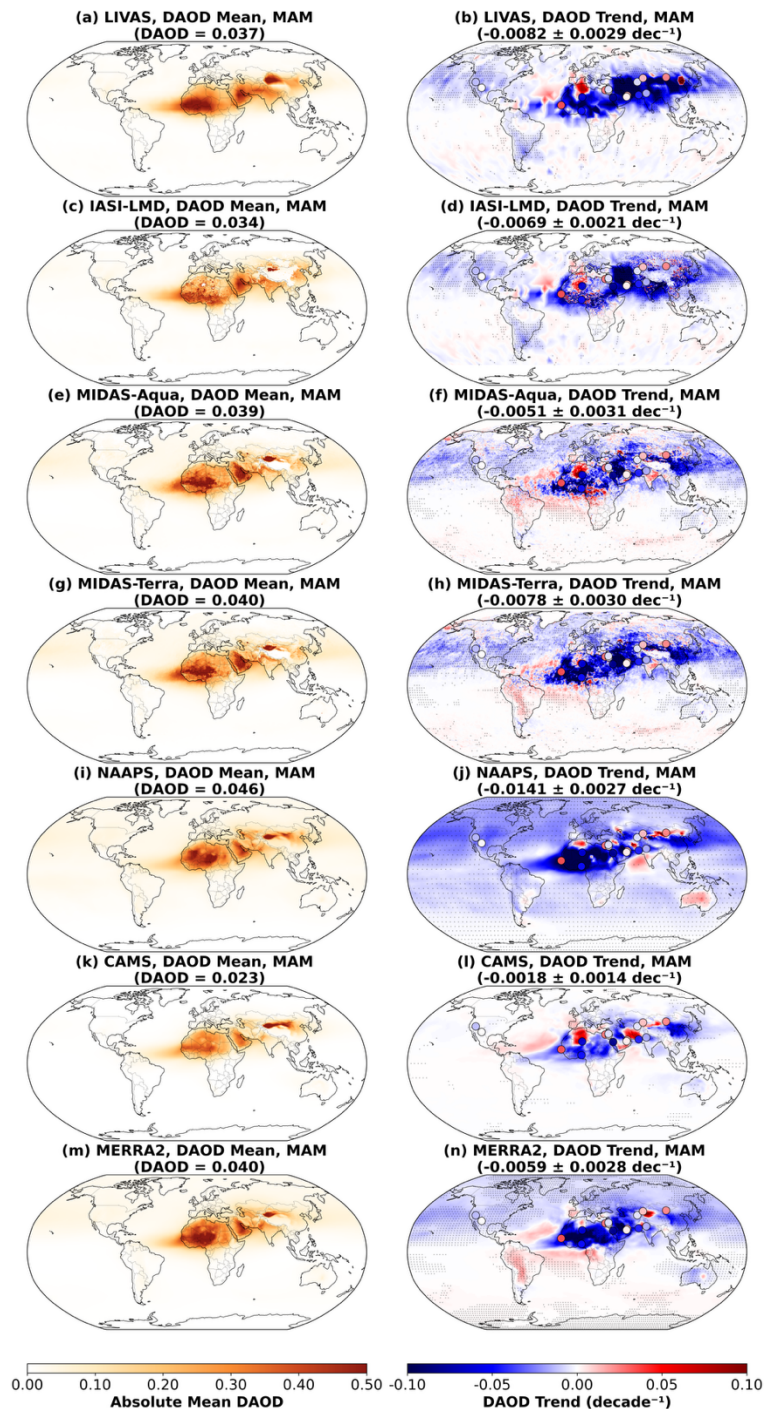
Supplementary Figure 4

Supplementary Figure 4: Trends in annual-mean dust aerosol optical depth (DAOD) over 2008–2021. *Heat map of linear trends in annual-mean DAOD for 2008–2021, shown as percentage change per decade (%dec⁻¹) relative to the 2008–2021 mean. Columns show regions (global mean at right) and rows show DAOD products (LIVAS, IASI–LMD, MIDAS, MIDAS–Terra, NAAPS, CAMS, MERRA-2 and the inverse-model estimate). Numbers in each cell indicate the regional trend with its one standard error.*

Supplementary *Figure 5: Global dust aerosol optical depth (DAOD) climatology and trends from satellite, reanalysis, and AERONET data during Northern Winter (DJF) season . Panels (a)-(g) show the annual mean DAOD at 550 nm for the overlapping period 2008-2021 from LIVAS (CALIPSO), IASI-LMD, MIDAS-Aqua, MIDAS-Terra, NAAPS, CAMS-RA, and MERRA-2. Panels (h)-(n) display the corresponding DAOD linear trends (decade^{-1}). Circles in (h) -(n) show the linear trends of conditionally filtered (see Methods) coarse-mode aerosol optical depth (AOD) derived from AERONET sun-photometer records at individual stations, as listed in Supplementary Table 1. Global area-weighted means and decadal trends are reported above each map. Small grey dots indicate grid cells where the linear DAOD trend is statistically significant at the 95% confidence level ($p < 0.05$).*
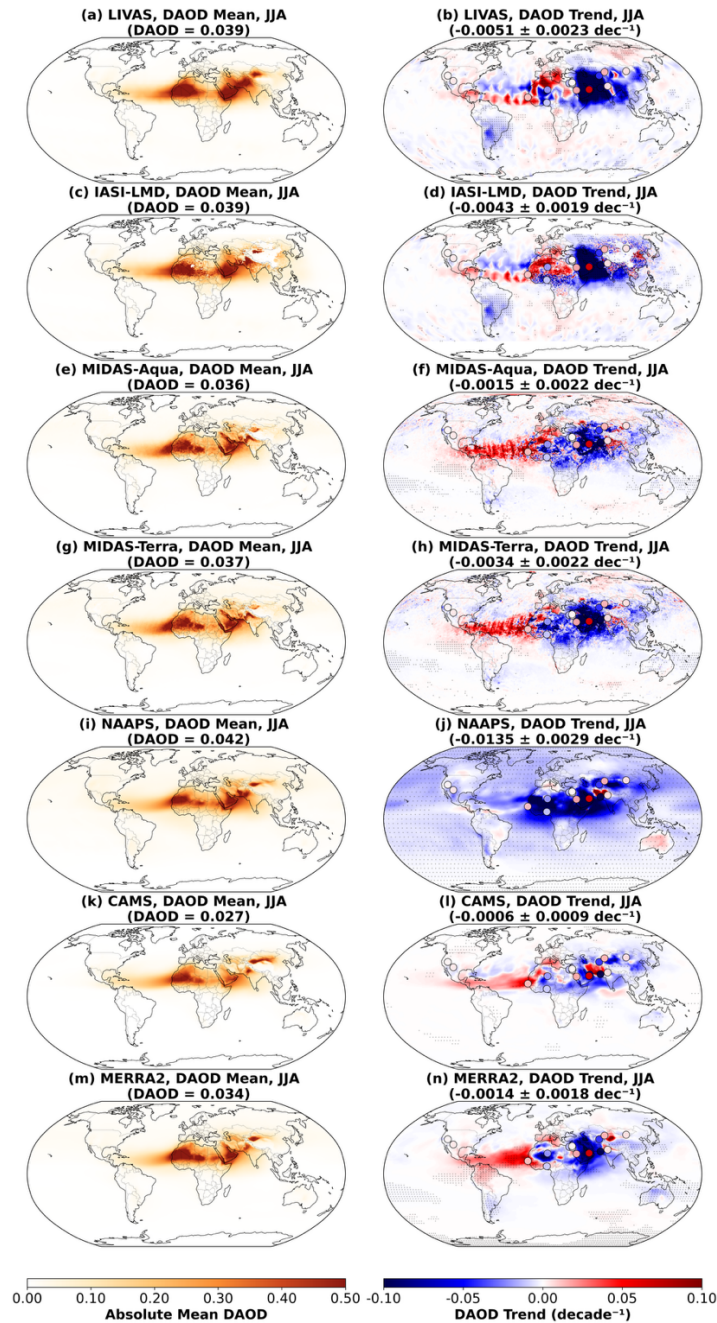
Supplementary *Figure 6*

(a) LIVAS, DAOD Mean, MAM (DAOD = 0.037)

(b) LIVAS, DAOD Trend, MAM (-0.0082 ± 0.0029 dec⁻¹)

(c) IASI-LMD, DAOD Mean, MAM (DAOD = 0.034)

(d) IASI-LMD, DAOD Trend, MAM (-0.0069 ± 0.0021 dec⁻¹)

(e) MIDAS-Aqua, DAOD Mean, MAM (DAOD = 0.039)

(f) MIDAS-Aqua, DAOD Trend, MAM (-0.0051 ± 0.0031 dec⁻¹)

(g) MIDAS-Terra, DAOD Mean, MAM (DAOD = 0.040)

(h) MIDAS-Terra, DAOD Trend, MAM (-0.0078 ± 0.0030 dec⁻¹)

(i) NAAPS, DAOD Mean, MAM (DAOD = 0.046)

(j) NAAPS, DAOD Trend, MAM (-0.0141 ± 0.0027 dec⁻¹)

(k) CAMS, DAOD Mean, MAM (DAOD = 0.023)

(l) CAMS, DAOD Trend, MAM (-0.0018 ± 0.0014 dec⁻¹)

(m) MERRA2, DAOD Mean, MAM (DAOD = 0.040)

(n) MERRA2, DAOD Trend, MAM (-0.0059 ± 0.0028 dec⁻¹)

0.00   0.10   0.20   0.30   0.40   0.50   -0.10   -0.05   0.00   0.05   0.10

Absolute Mean DAOD   **DAOD Trend (decade⁻¹)**

Supplementary *Figure 6: Global dust aerosol optical depth (DAOD) climatology and trends from satellite, reanalysis, and AERONET data during Northern Spring (MAM) season . Panels (a)-(g) show the annual? mean DAOD at 550 nm for the overlapping period 2008-2021 from LIVAS (CALIPSO), IASI-LMD, MIDAS-Aqua, MIDAS-Terra, NAAPS, CAMS-RA, and MERRA-2. Panels (h)-(n) display the corresponding DAOD linear trends (decade⁻¹). Circles in (h) -(n) show the linear trends of conditionally filtered (see Methods) coarse-mode aerosol optical depth (AOD) derived from AERONET sun-photometer*

records at individual stations, as listed in Supplementary Table 1. Global area-weighted means and decadal trends are reported above each map. Small grey dots indicate grid cells where the linear DAOD trend is statistically significant at the 95% confidence level (p < 0.05).
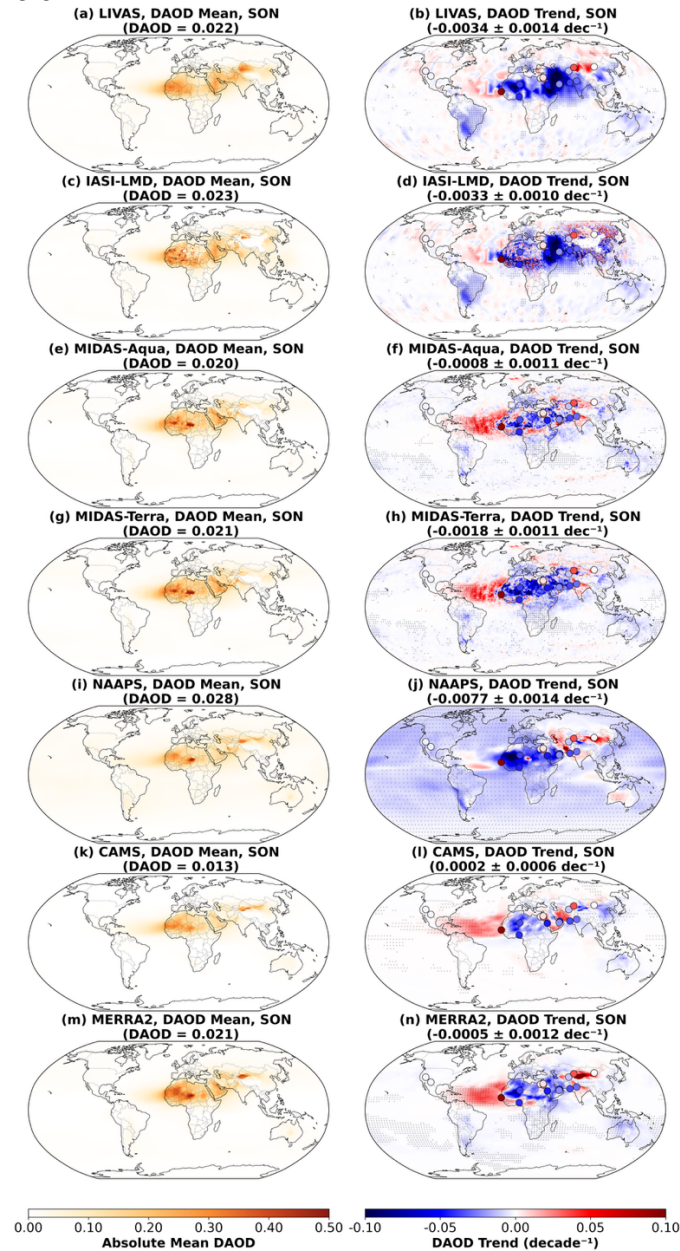
Supplementary *Figure 7*

Supplementary *Figure 7*: *Global dust aerosol optical depth (DAOD) climatology and trends from satellite, reanalysis, and AERONET data during Northern Summer (JJA) season . Panels (a)-(g) show the annual? mean DAOD at 550 nm for the overlapping period 2008-2021 from LIVAS (CALIPSO), IASI-LMD, MIDAS-Aqua, MIDAS-Terra, NAAPS, CAMS-RA, and MERRA-2. Panels (h)-(n) display the*

corresponding DAOD linear trends (decade⁻¹). Circles in (h) -(n) show the linear trends of conditionally filtered (see Methods) coarse-mode aerosol optical depth (AOD) derived from AERONET sun-photometer records at individual stations, as listed in Supplementary Table 1. Small grey dots indicate grid cells where the linear DAOD trend is statistically significant at the 95% confidence level (p < 0.05).
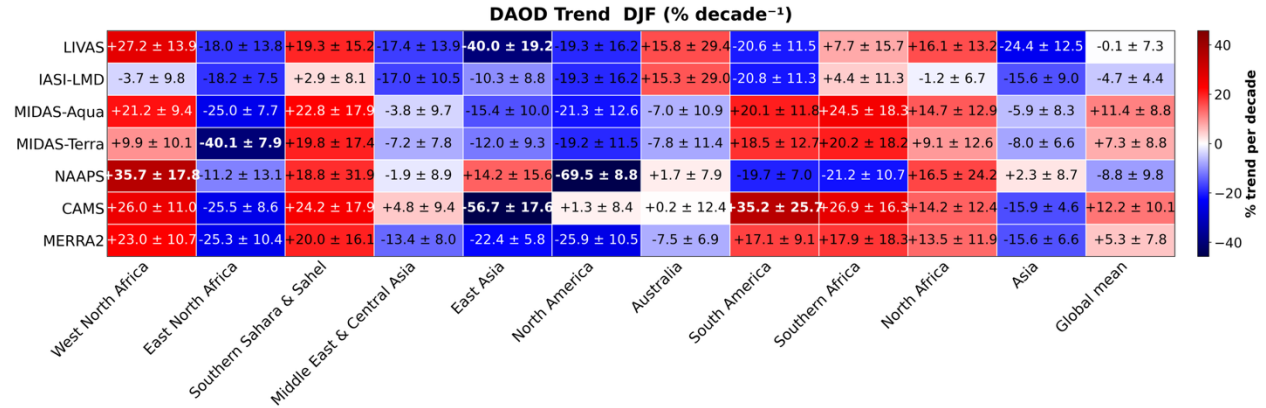
Supplementary *Figure 8*

Supplementary *Figure 8*: *Global dust aerosol optical depth (DAOD) climatology and trends from satellite, reanalysis, and AERONET data during Northern Autumn (SON) season .* *Panels (a)-(g) show the annual? mean DAOD at 550 nm for the overlapping period 2008-2021 from LIVAS (CALIPSO), IASI-LMD, MIDAS-Aqua, MIDAS-Terra, NAAPS, CAMS-RA, and MERRA-2. Panels (h)-(n) display the corresponding DAOD linear trends (decade⁻¹). Circles in (h) -(n) show the linear trends of conditionally filtered (see Methods) coarse-mode aerosol optical depth (AOD) derived from AERONET sun-photometer*
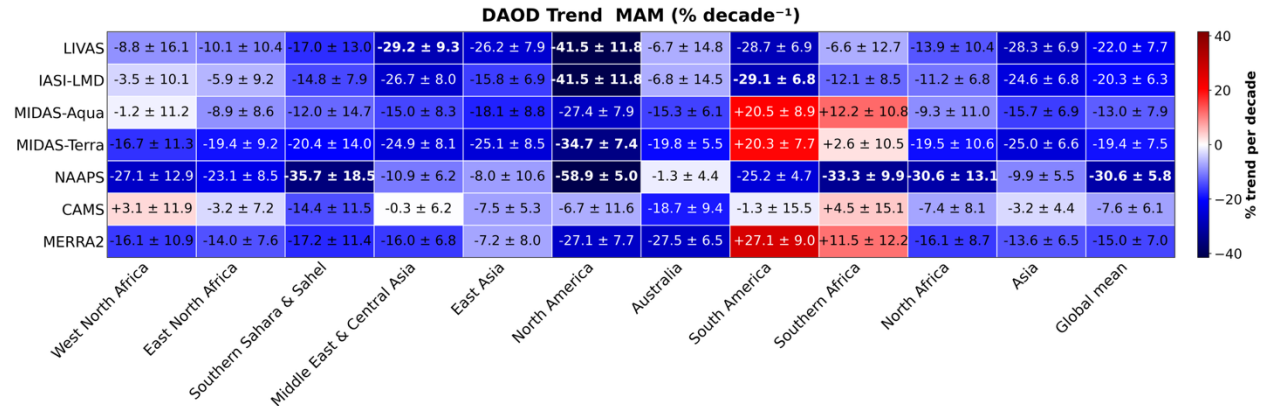
records at individual stations, as listed in Supplementary Table 1. Small grey dots indicate grid cells where the linear DAOD trend is statistically significant at the 95% confidence level (p < 0.05).

Supplementary *Figure 9*

Supplementary Figure 9: Trends in Northern winter dust aerosol optical depth (DAOD) over 2008–2021. *Heat map of linear trends in Northern winter DAOD for 2008–2021, shown as percentage change per decade (%dec⁻¹) relative to the 2008–2021 mean.*
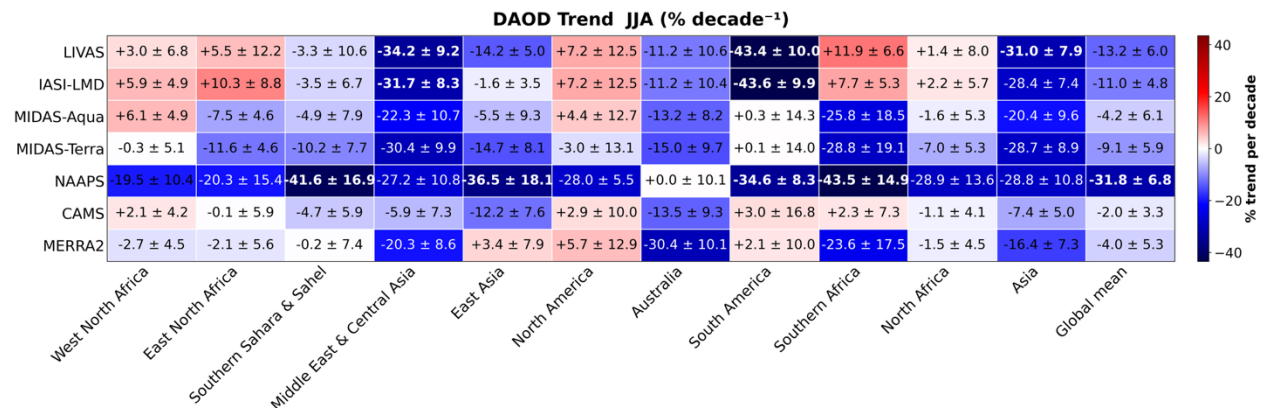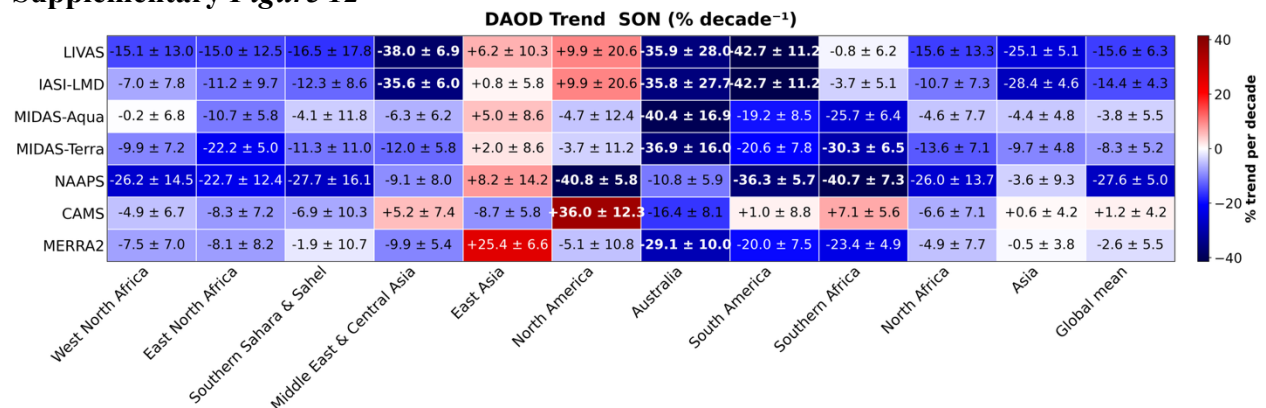
Supplementary *Figure 10*

Supplementary Figure 10: Trends in Northern spring (MAM) dust aerosol optical depth (DAOD) over 2008–2021. *Heat map of linear trends in Northern* **spring** *DAOD for 2008–2021, shown as percentage change per decade (%dec⁻¹) relative to the 2008–2021 mean.*

DAOD Trend JJA (% decade⁻¹)

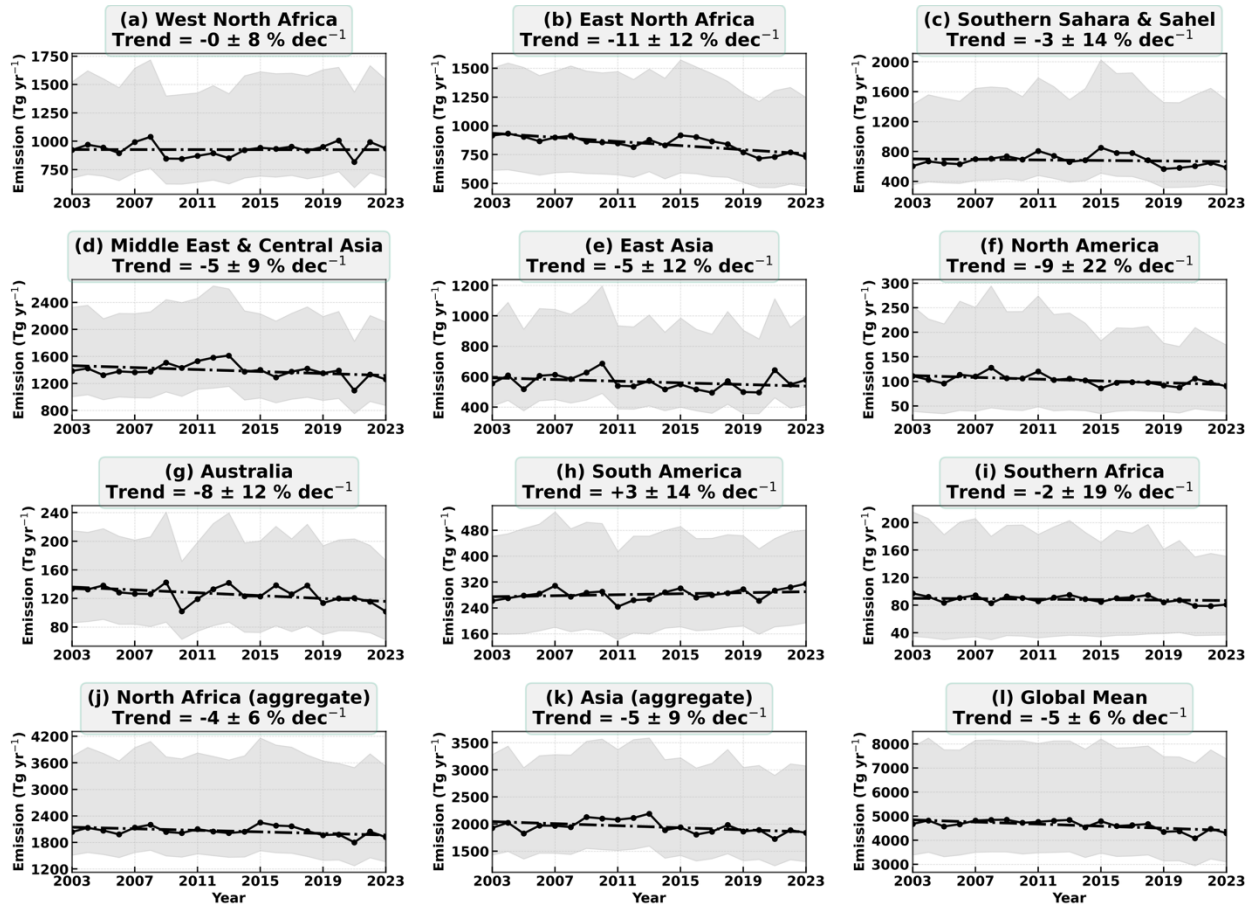|	West North Africa	East North Africa	Southern Sahara & Sahel	Middle East & Central Asia	East Asia	North America	Australia	South America	Southern Africa	North Africa	Asia	Global mean
LIVAS	+3.0 ± 6.8	+5.5 ± 12.2	-3.3 ± 10.6	**-34.2 ± 9.2**	-14.2 ± 5.0	+7.2 ± 12.5	-11.2 ± 10.6	**-43.4 ± 10.0**	+11.9 ± 6.6	+1.4 ± 8.0	**-31.0 ± 7.9**	-13.2 ± 6.0
IASI-LMD	+5.9 ± 4.9	+10.3 ± 8.8	-3.5 ± 6.7	**-31.7 ± 8.3**	-1.6 ± 3.5	+7.2 ± 12.5	-11.2 ± 10.4	**-43.6 ± 9.9**	+7.7 ± 5.3	+2.2 ± 5.7	-28.4 ± 7.4	-11.0 ± 4.8
MIDAS-Aqua	+6.1 ± 4.9	-7.5 ± 4.6	-4.9 ± 7.9	-22.3 ± 10.7	-5.5 ± 9.3	+4.4 ± 12.7	-13.2 ± 8.2	+0.3 ± 14.3	-25.8 ± 18.5	-1.6 ± 5.3	-20.4 ± 9.6	-4.2 ± 6.1
MIDAS-Terra	-0.3 ± 5.1	-11.6 ± 4.6	-10.2 ± 7.7	-30.4 ± 9.9	-14.7 ± 8.1	-3.0 ± 13.1	-15.0 ± 9.7	+0.1 ± 14.0	-28.8 ± 19.1	-7.0 ± 5.3	-28.7 ± 8.9	-9.1 ± 5.9
NAAPS	-19.5 ± 10.4	-20.3 ± 15.4	-41.6 ± 16.9	-27.2 ± 10.8	-36.5 ± 18.1	-28.0 ± 5.5	+0.0 ± 10.1	**-34.6 ± 8.3**	-43.5 ± 14.9	-28.9 ± 13.6	-28.8 ± 10.8	**-31.8 ± 6.8**
CAMS	+2.1 ± 4.2	-0.1 ± 5.9	-4.7 ± 5.9	-5.9 ± 7.3	-12.2 ± 7.6	+2.9 ± 10.0	-13.5 ± 9.3	+3.0 ± 16.8	+2.3 ± 7.3	-1.1 ± 4.1	-7.4 ± 5.0	-2.0 ± 3.3
MERRA2	-2.7 ± 4.5	-2.1 ± 5.6	-0.2 ± 7.4	-20.3 ± 8.6	+3.4 ± 7.9	+5.7 ± 12.9	-30.4 ± 10.1	+2.1 ± 10.0	-23.6 ± 17.5	-1.5 ± 4.5	-16.4 ± 7.3	-4.0 ± 5.3

Supplementary Figure 11: Trends in Northern summer (JJA) dust aerosol optical depth (DAOD) over 2008–2021. *Heat map of linear trends in Northern **summer** DAOD for 2008–2021, shown as percentage change per decade (%dec⁻¹) relative to the 2008–2021 mean.*

DAOD Trend SON (% decade⁻¹)

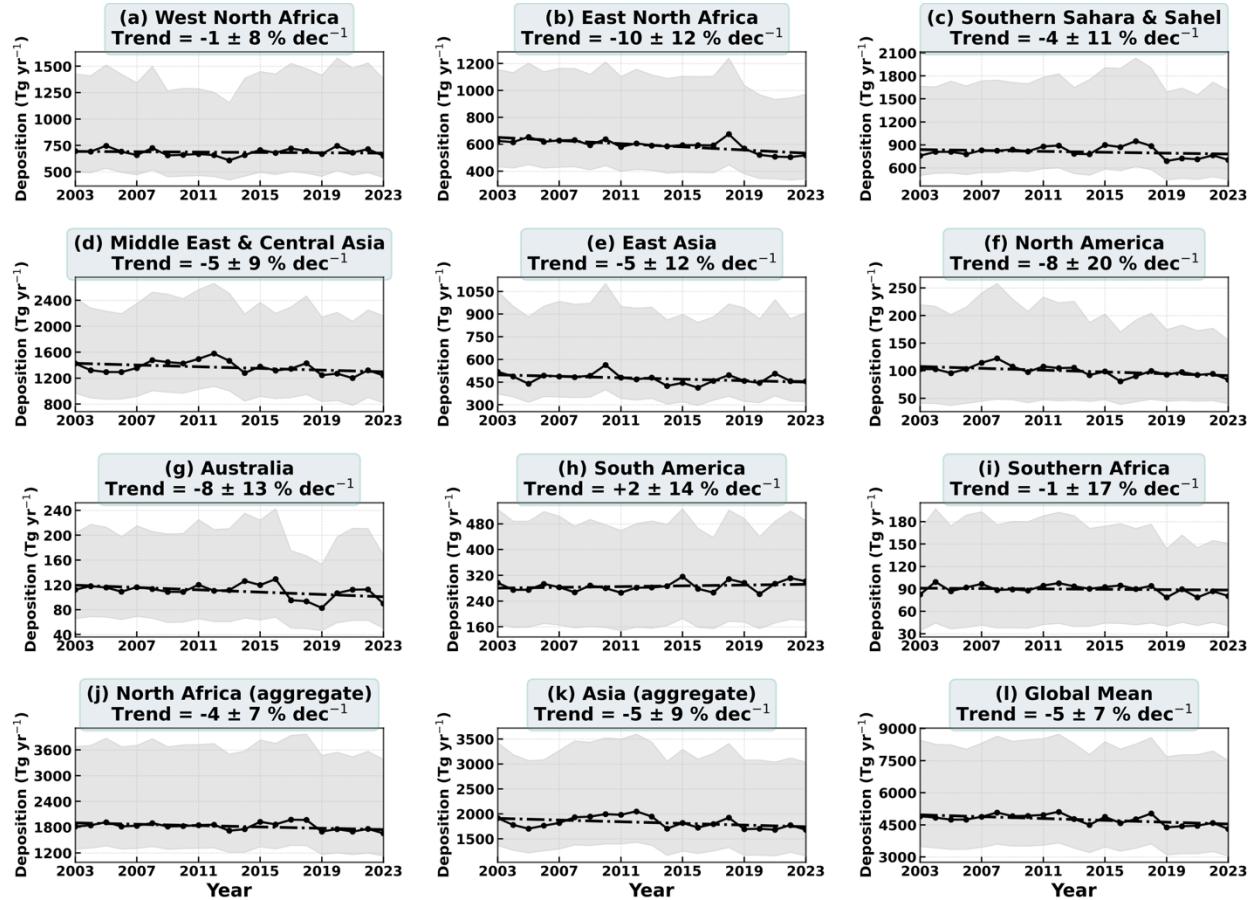|	West North Africa	East North Africa	Southern Sahara & Sahel	Middle East & Central Asia	East Asia	North America	Australia	South America	Southern Africa	North Africa	Asia	Global mean
LIVAS	-15.1 ± 13.0	-15.0 ± 12.5	-16.5 ± 17.8	**-38.0 ± 6.9**	+6.2 ± 10.3	+9.9 ± 20.6	**35.9 ± 28.0**	**42.7 ± 11.2**	-0.8 ± 6.2	-15.6 ± 13.3	-25.1 ± 5.1	-15.6 ± 6.3
IASI-LMD	-7.0 ± 7.8	-11.2 ± 9.7	-12.3 ± 8.6	**-35.6 ± 6.0**	+0.8 ± 5.8	+9.9 ± 20.6	**35.8 ± 27.7**	**42.7 ± 11.2**	-3.7 ± 5.1	-10.7 ± 7.3	-28.4 ± 4.6	-14.4 ± 4.3
MIDAS-Aqua	-0.2 ± 6.8	-10.7 ± 5.8	-4.1 ± 11.8	-6.3 ± 6.2	+5.0 ± 8.6	-4.7 ± 12.4	**40.4 ± 16.9**	-19.2 ± 8.5	-25.7 ± 6.4	-4.6 ± 7.7	-4.4 ± 4.8	-3.8 ± 5.5
MIDAS-Terra	-9.9 ± 7.2	-22.2 ± 5.0	-11.3 ± 11.0	-12.0 ± 5.8	+2.0 ± 8.6	-3.7 ± 11.2	**36.9 ± 16.0**	-20.6 ± 7.8	**-30.3 ± 6.5**	-13.6 ± 7.1	-9.7 ± 4.8	-8.3 ± 5.2
NAAPS	-26.2 ± 14.5	-22.7 ± 12.4	-27.7 ± 16.1	-9.1 ± 8.0	+8.2 ± 14.2	**-40.8 ± 5.8**	-10.8 ± 5.9	**-36.3 ± 5.7**	**-40.7 ± 7.3**	-26.0 ± 13.7	-3.6 ± 9.3	**-27.6 ± 5.0**
CAMS	-4.9 ± 6.7	-8.3 ± 7.2	-6.9 ± 10.3	+5.2 ± 7.4	-8.7 ± 5.8	**36.0 ± 12.3**	-16.4 ± 8.1	+1.0 ± 8.8	+7.1 ± 5.6	-6.6 ± 7.1	+0.6 ± 4.2	+1.2 ± 4.2
MERRA2	-7.5 ± 7.0	-8.1 ± 8.2	-1.9 ± 10.7	-9.9 ± 5.4	**+25.4 ± 6.6**	-5.1 ± 10.8	**-29.1 ± 10.0**	-20.0 ± 7.5	-23.4 ± 4.9	-4.9 ± 7.7	-0.5 ± 3.8	-2.6 ± 5.5

Supplementary Figure 12: Trends in Northern autumn (SON) dust aerosol optical depth (DAOD) over 2008–2021. *Heat map of linear trends in Northern **autumn** DAOD for 2008–2021, shown as percentage change per decade (%dec⁻¹) relative to the 2008–2021 mean.*
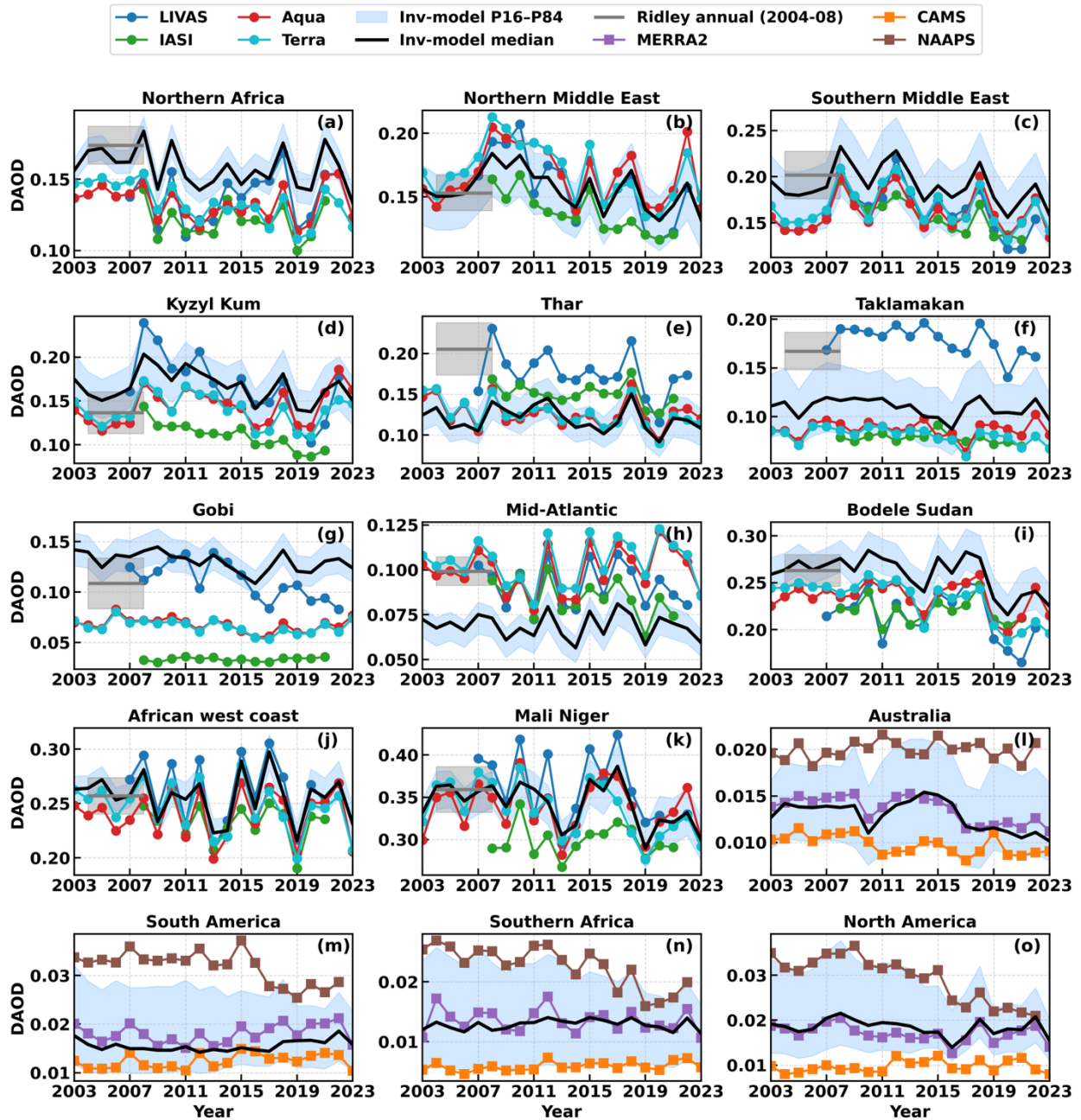
Supplementary *Figure 13*

Supplementary *Figure 13*. *Inverse-model–based reconstruction of regional and global dust emissions, 2003–2023*: *Annual inverse-model–based dust emission fluxes from 2003 to 2023 in nine source regions (panels a–i), two aggregated domains over North Africa and Asia (panels j–k), and all nine sources combined (panel l). The black line represents the inverse-model median of dust emission (Tg yr^{-1}). The brown line represents the relative changes in the inverse-model median of dust emission (Tg yr^{-1}), with shading indicating the ±1σ (16th–84th percentile; P16–P84) range. The gray dashed-dotted line indicates the trend, and the inset panel shows the estimated trend per decade based on the relative changes in the inverse-model median of dust emission from 2003 to 2023.*

Supplementary *Figure 14*

Supplementary *Figure 14. Inverse-model–based reconstruction of regional and global dust deposition fluxes, 2003–2023*: *Annual inverse-model–based dust deposition from 2003 to 2023 in nine source regions (panels a–i), two aggregated domains over North Africa and Asia (panels j–k), and over globe (panel l). The black line represents the inverse-model median of dust deposition (Tg yr^{-1}). The brown line represents the relative changes in the inverse-model median of dust deposition (Tg yr^{-1}), with shading indicating the ±1σ (16th–84th percentile; P16–P84) range. The gray dashed-dotted line indicates the trend, and the inset panel shows the estimated trend per decade based on the relative changes in the inverse-model median of dust deposition from 2003 to 2023. Note that the deposition values here represent the flux of dust depositing within each region, not dust originating from each region.*

Supplementary Figure 15

Supplementary Figure 15. Regional annual dust aerosol optical depth (DAOD) time series and inverse model results (2003–2023) *for the 15 dusty regions. Observations are plotted as solid lines for LIVAS (blue circles), IASI (green circles), Aqua (red circles), and Terra (cyan circles). Reanalysis products are plotted as solid lines for MERRA-2 (purple squares), CAMS (orange squares), and NAAPS (brown squares). The inverse-model reconstruction is represented by the ensemble median (black line), with blue shading bands denoting the ±1σ (16th–84th percentile) range. For selected regions, seasonal and annual means from Ridley et al. (2004–2008) are*

overlaid as horizontal gray bars with uncertainty envelopes. Panels (a–o) correspond to the 15 source regions defined in the Methods and Supplementary Figure 1.

Supplementary Table 1

Datasets	LIVAS	MIDAS-Aqua-PM/Terra-AM	IASI-LMD	NAAPS	CAMS	MERRA-2
Time Period	**2007-2022**	**2003-2023**	**2008-2021**	**2003-2023**	**2003-2023**	**2003-2023**
Spatial/ Temporal Resolution	**Horizontal: 1°** (Vertical: ~60 m bins below 20 km)	**~0.1°** (~10 km), daily swaths	**Footprints ~12 km** Daily mapping ~0.5° (with interpolation)	**~1° grid** 6-hourly outputs	**~0.7° grid** 3-hourly outputs	**~0.5° grid** 3-hourly outputs
Coverage	**Global but sparse** (narrow orbital track); monthly averaging often needed)	**Global, wide-swath** coverage (1–2 overpasses per day	**Global** (2 overpasses per day), nighttime retrievals possible	**Global, continuous** coverage (no data gaps-model filled)	**Global** coverage with continuous fields over multiple years	Global coverage extends back to 1980 (long record)

Supplementary Table 1. Comparison of aerosol datasets and their characteristics for six DAOD products (LIVAS, MIDAS-Aqua-PM/Terra-AM, IASI-LMD, NAAPS, CAMS, MERRA-2). *We detail the available time periods, spatial and temporal resolutions (ranging from coarse ~0.5°-1° grids and narrow orbital tracks to high-resolution daily swaths and 3-hourly outputs), global coverage nuances, and associated accuracy and uncertainty metrics, including comparisons to AERONET measurements. Note that we used a harmonized 0.5° × 0.5° grid for all seven products as input to the inverse model.*